Electronic supplementary information for

Strain engineering of Bi_2OS_2 ultrathin films: electronic and ferroelectric properties

Chunying Pang [1], Kai Gao,[1] Chunju Hou[2], Yi Yang,[1]*

[1] College of Rare Earths and Faculty of Materials, Metallurgy and Chemistry, Jiangxi University of Science and Technology, Ganzhou, 341000, China

[2] School of Science, Jiangxi University of Science and Technology, Ganzhou, 341000, China

*Corresponding author, e-mail address: yangyisouth@yeah.net

ESI Section S1: structural properties

A. Effect of vdW on structural optimization

Since the bulk and multilayers are composed of basic units via Van der Waals (vdW) interaction along c-axis, test calculations including vdW-correction are done to confirm the conclusions made by PBE method. We find that vdW-correction does not change the main conclusions obtained from PBE method. The test calculations are performed in three steps.

First, we optimize the structures of bilayer, trilayer and bulk Bi_2OS_2 by utilizing DFT+D3 (here, PBE+D3) and vdW-DF (here, optPBE-vdW), which are two typical methods to consider vdW correction.[1-3] The lattice parameters are listed together with the results from PBE functional in Table. S1. It is seen that the lattice constants calculated from these two methods with vdW correction agree well with those from PBE functional, indicating a good accuracy of PBE in calculating the structural parameters of Bi_2OS_2. We note that PBE+D3 gives rise to less error for lattice parameters with respect to experimental data, i.e., 0% of error for a and +1.5% for c, than PBE (+0.5% and +3.1% of error for a and c, respectively). Then, we calculate the band gaps of bilayer and trilayer at typical biaxial strain conditions (-4%, 0% and 4%) by using PBE+D3 and optPBE-vdW. We find that the band gaps calculated from these two methods are close to corresponding PBE-gaps (Table. S2). These three methods provide a consistent trend of the band gaps, i.e., a significant enhancement of the gap value with compressive strain and a slight increase with tensile strain. Finally, we calculate the energy difference (ΔE) between PE and FE structures and the FE polarizations by using optPBE-vdW for bilayer. It is seen that the ΔE values and the FE polarizations calculated from PBE and optPBE-vdW are consistent with each other (Fig. S1). Either for the ΔE or the FE polarization, the varying trend with strain obtained from PBE are well-reproduced by optPBE-vdW. Most important of all, the non-monotonous trend of the polarization and the nearly monotonously strain-dependent ΔE are fully reproduced by using optPBE-vdW. All in all, we believe that PBE is an accurate method in calculating the electronic and FE properties of Bi_2OS_2 monolayer and multilayers.

Table. S1 Lattice parameters (*a* and *c*, Å) of the bulk and 2D Bi$_2$OS$_2$ calculated by PBE, PBE+D3 and optPBE-vdW methods. The bulk crystalizes in a tetragonal phase (space group: P4/nmm) at ambient condition. The angles α, β and γ are all 90°. In 2D Bi$_2$OS$_2$, the angles remain 90° and in-plane lattice constants (a = b) are listed here. The experimental parameters (Expt.) of the bulk are also listed for a comparison (taken from ref. 4).

	PBE	PBE+D3	optPBE-vdW	Expt.
Monolayer-*a*	3.967			
Bilayer-*a*	3.975	3.957	3.992	
Trilayer-*a*	3.977	3.963	3.994	
Bulk-*a*	3.981	3.961	4.000	3.961
Bulk-*c*	14.224	14.008	14.185	13.802

Table. S2 Band gaps (eV) calculated by PBE, PBE+D3 and optPBE-vdW methods for PE bilayer and trilayer at -4%, 0% and 4% strains. The band gap of the bulk is also calculated with these methods.

	Strains	PBE	PBE+D3	vdW-DF
Bilayer	-4%	1.16	1.08	1.18
	0%	0.80	0.75	0.82
	4%	0.82	0.85	0.90
Trilayer	-4%	1.06	1.02	1.05
	0%	0.72	0.75	0.68
	4%	0.79	0.85	0.77
Bulk		0.96	1.02	0.97

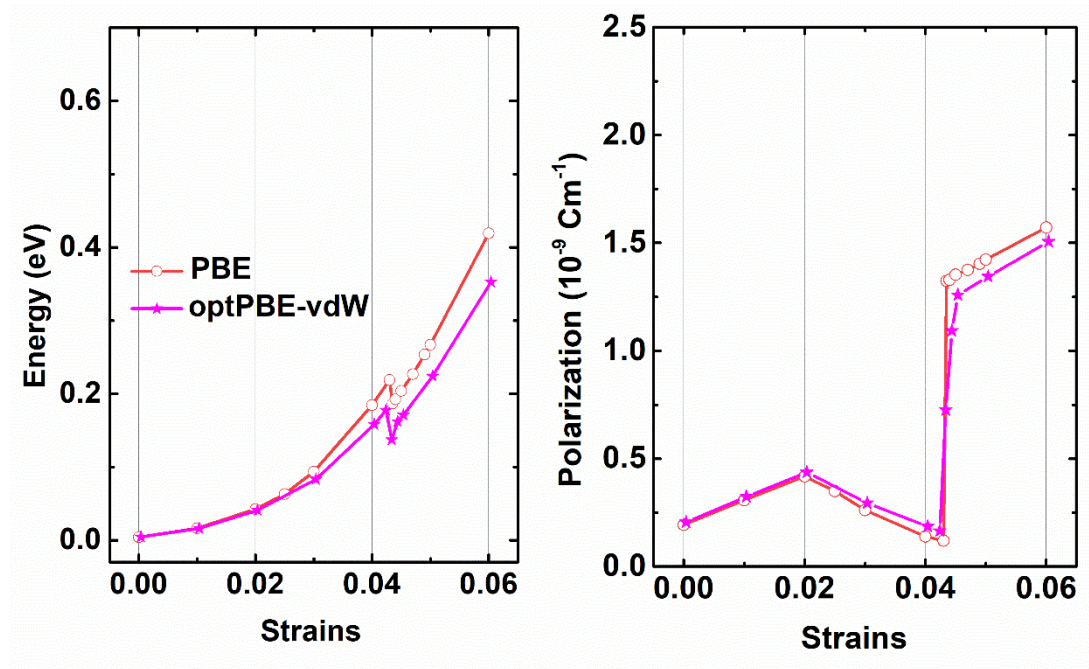**Fig. S1** FE stability (ΔE) and polarization of Bi$_2$OS$_2$ bilayer as function of biaxial strain calculated by using PBE and optPBE-vdW methods.

B . *Structural models and bond lengths of monolayer with/without strain*

Fig. S2 displays the structural models of the coordination environments and chemical bonds of Bi and S atoms. Fig. S3 shows the PE and FE structural models of monolayer at typical strains (-6%, -4%, 0%, 4% and 6%). It is seen that monolayer do not corrugate upon compression and expansion in the strain range of (-6%, 6%), as indicated by the flat [Bi_2O_2] layer. However, the strain makes a difference to the displacement of S_{xy} along the out-of-plane direction (*c*-axis). Without strain, the S_{xy} atoms sit on higher positions than the Bi atoms about 0.48 Å (i.e., *c*-coordinate difference between S_{xy} and Bi) in the top [BiS_2] layer (or lower with same distance of 0.48 Å in the bottom [BiS_2] layer). The *c*-coordinate difference increases to 0.86 Å for -6% strain, and decreases to 0.22 Å for 6% strain. Fig. S3 also shows the FE structures of monolayer for 4% and 6% tensile strain (at compressive strain, FE structures are not ground states), where no corrugates appear.

We list the bond lengths in Table. S3. To obtain a reasonable understanding about the Bi-S and Bi-O bonds in the strained structures, we make a comparison of Bi-S/O bond lengths with a sum (d_{cov}, Å) of the covalent radii of Bi and S (or O) atoms, and with a sum (d_{vdW}, Å) of their vdW radii. We find that, in the strain range of (-6%, 6%), the bond lengths of Bi^*-O are close to the d_{cov} of Bi and O, suggesting covalent bonding interaction between Bi^* and O. The bond lengths of Bi-S_z are also close to the sum of the covalent radii of Bi and S. Bi-S_{xy} and Bi^*-S_z show longer bond lengths at the ranges of (2.772, 2.981) Å and (3.056, 3.241) Å, respectively. The lengths of Bi-S_{xy} and Bi^*-S_z are longer than the d_{cov}, while being much shorter than the d_{vdW}, indicating that these two kinds of bonds also tend to exhibit covalent bonding interaction, rather than the vdW interaction. In a word, these bonds can be reasonably described as chemical bonds.

Table. S3 Bond lengths (Å) of Bi-S_{xy}, Bi-S_z, Bi^*-S_z and Bi^*-O for PE monolayer as a function of strain. The sum (d_{cov}, Å) of the covalent radii (r_{cov}, Å) of Bi and S (or O) atoms and the sum (d_{vdW}, Å) of their vdW radii (r_{vdW}, Å) are also listed here. The values of r_{cov} for Bi, O and S are 1.48, 0.66 and 1.05 Å (ref. 5). The values of r_{vdW} for Bi, O and S are 2.3, 1.55 and 1.8 Å (ref. 6). The structural models of these bonds are displayed in Fig. S2.

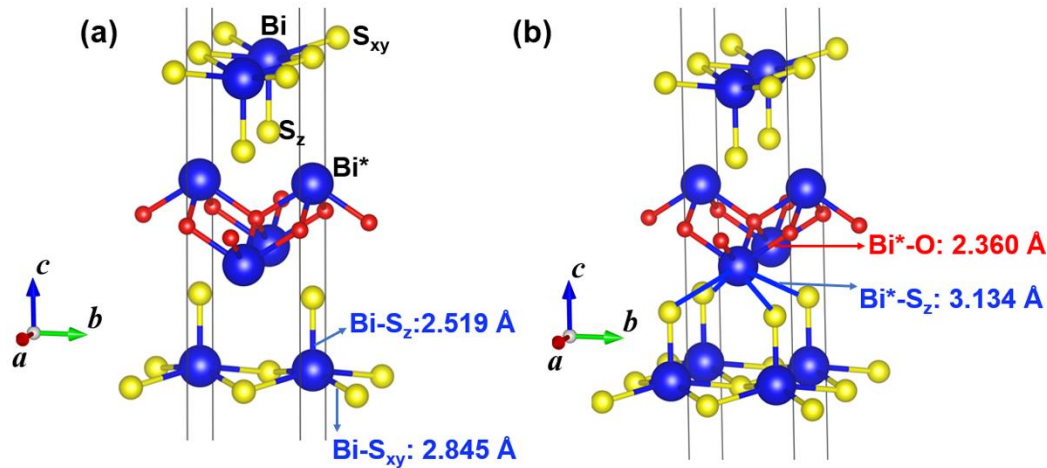| Strains	Bi-S_{xy}	Bi-S_z	Bi^*-S_z	Bi^*-O
-0.06	2.772	2.554	3.056	2.305
-0.04	2.785	2.541	3.077	2.322
-0.02	2.810	2.530	3.103	2.341
0	2.845	2.519	3.134	2.360
0.02	2.886	2.507	3.164	2.379
0.04	2.933	2.496	3.199	2.399
0.06	2.981	2.483	3.241	2.419
d_{cov}	2.53			2.14
d_{vdW}	4.1			3.85

Fig. S2 (a) a perspective view of the structural model for PE monolayer (0% strain). It is seen that in a [BiS$_2$] layer, one Bi atom coordinates with five S atoms in a tetragonal pyramid configuration. To indicate the coordination environment of Bi atom in a [Bi$_2$O$_2$] layer, the bottom [BiS$_2$] layer is doubled along **a**-axis, as is shown in (b). One Bi atom (denoted as Bi*) in a [Bi$_2$O$_2$] layer coordinates with four O atoms and four S atoms in a nearly eight-coordination configuration. The bond lengths of Bi-S$_z$, Bi-S$_{xy}$, Bi*-O and Bi*-S$_z$ are marked by the numbers.
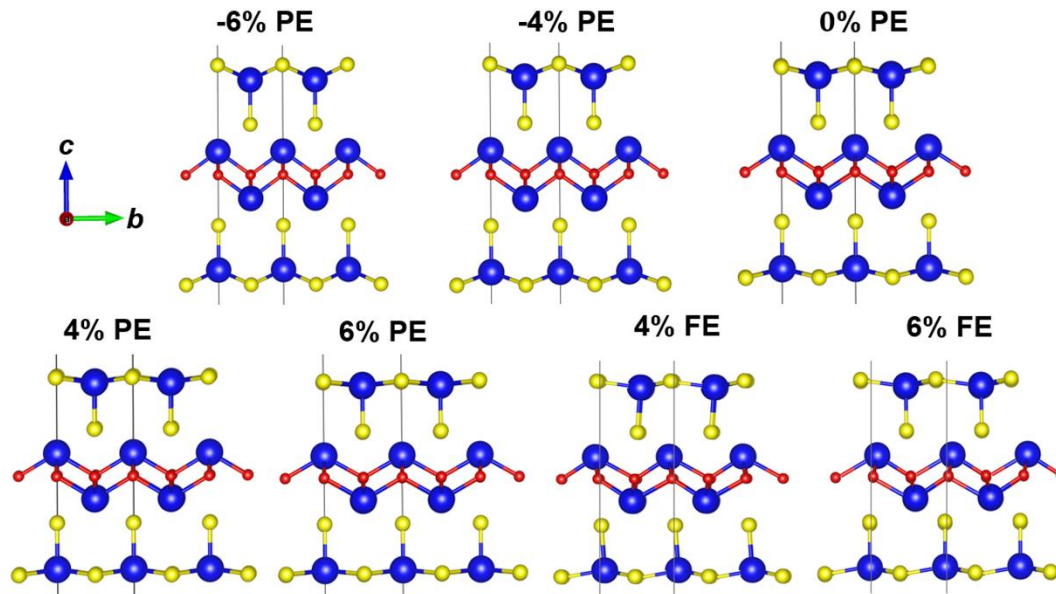

Fig. S3 PE structural models of monolayer at typically strains (-6%, -4%, 0%, 4% and 6%); FE structural models for 4% and 6% tensile strain.

ESI Section S2: electronic structures and band gaps

In this section, we first discuss the effect of exchange-correlation functional on the band gaps. We then check the convergence criteria of atomic forces and k-point mesh by inspecting the electronic structures. Finally, we discuss the band structures and band gaps of 2D Bi$_2$OS$_2$, including the meaning of small deviation of CBM from X and orbital projected band structures of monolayer.

A. *Effect of exchange-correlation functional on the band gaps.*

Table. S4 lists the band gaps (eV) of monolayer (0% strain) and bulk Bi_2OS_2 calculated by using PBE, HSE06 and PBE0 with (+SOC) and without SOC. Hybrid functional including some exact exchange component (25% for HSE06) usually enlarge the calculated band gaps in comparison with PBE functional, as seen from Table. S4. In contrast, the SOC effect reduces the band gaps, which mostly originates from the band splitting of the CBM since Bi 6p states dominate the CBM. A cancellation of these two factors results in close gap values between HSE06+SOC and PBE, indicating a reasonable accuracy of PBE in predicting the band gaps for Bi_2OS_2. In Fig. 2b of the main text, the SOC effect on the gap reduction is more significant than the gap increase factor of hybrid functional, giving rise to slightly smaller band gap for HSE06+SOC method than PBE-gap.

Overall, the band-gap values from PBE and HSE06+SOC are consistent with each other and closer to the experimental value than other methods including PBE0 and PBE0+SOC. We then use the PBE method to obtain the trends of band gaps considering that HSE06+SOC is high-consuming in computing resource.

Table. S4 Band gaps (eV) of monolayer (0% strain) and bulk Bi_2OS_2 calculated by using PBE, HSE06 and PBE0 with (+SOC) and without SOC. The experimental value of the bulk is also listed here for a comparison (from ref. 4).

Band gap	PBE	PBE+SOC	HSE06	HSE06+SOC	PBE0	PBE0+SOC	Expt.
Monolayer	1.02	0.54	1.43	0.84	2.03	1.45	
Bulk	0.96	0.61	1.44	0.89	2.00	1.53	0.99

B. *Convergence criteria of atomic forces*

We have checked that a force tolerance of 0.01 eV/Å is accurate enough to ensure the convergence of our results. The present results are compared with those obtained from a tolerance of 0.001 eV/Å. We optimized the PE and FE structures of monolayer by using a tolerance of 0.001 eV/Å at typical strain conditions: -4%, 0%, +4%, and calculated the band gaps for these structures. The results from two force tolerances are presented together in the following Table. S5. It is seen that the largest relative error for the band gaps, one of the main quantities we focus on, is 1.02%, indicating the good convergences of the gap values. The largest absolute error is 0.0104 eV occurring to the 0% strain PE structure, which is lower than the errors or the discrepancies of experimental gap values measured from optical spectra for common semiconductors.[7] For example, the errors of experimental gap values (i.e., the data dispersion of gap values), which may originate from different sets of measurements and/or analyses, are typically around 0.01~0.08 eV for Si, Ge and GaAs (see Figure 2 of ref. 7).[7] The discrepancies due to different analysis methods in determining the gap values are about 0.06~0.2 eV for Si, Ge and GaAs. Thus, a force tolerance of 0.01 eV/Å is accurate enough to ensure the convergence of the band gaps. The convergence of FE properties with respect to force tolerance is discussed in **ESI Section S4.**

Table. S5 Band gaps (E_g, eV) of the PE and FE structures of monolayer calculated by using two force tolerances of 0.01 eV/Å and 0.001 eV/Å to optimize the structure. The absolute errors (Δ_A, eV) and relative errors (Δ_R, %) are also listed in the last row.

Cases	-4% strain		0% strain		4% strain	
	PE	FE	PE	FE	PE	FE
E_g (0.01)	1.3423	1.3454	1.0213	1.0370	1.0382	1.1514
E_g (0.001)	1.3448	1.3448	1.0109	1.0270	1.0348	1.1431
Δ_A (eV)	-0.0025	0.0006	0.0104	0.0100	0.0034	0.0083
Δ_R (%)	-0.19	0.04	1.02	0.96	0.33	0.72

C. Choice of k-point mesh

To indicate the convergence of the results with respect to k-point mesh, we calculate the electronic structures (including the band gaps and band edges) of monolayer by utilizing a denser k-point mesh (8×8×1) (Fig. S4). It is seen that the band gaps and the band edges of monolayer, either for PE or FE configuration, converge well by using the present mesh 6×6×1. Also, the present mesh is accurate enough to reproduce the energy difference (ΔE) between PE and FE monolayer.
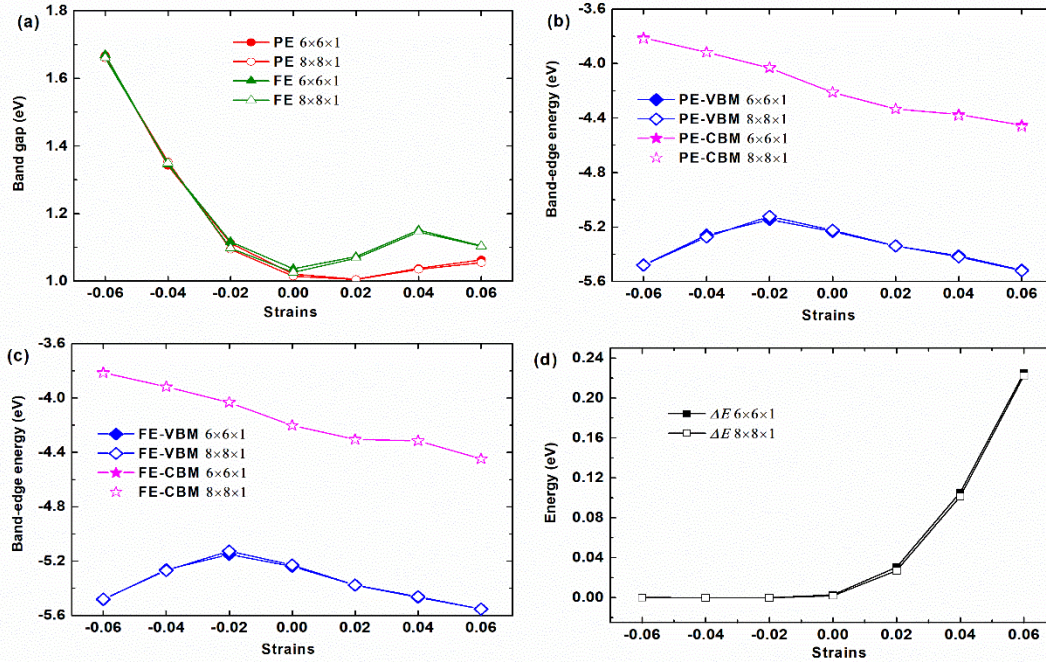

Fig. S4 Test calculations using 6×6×1 and 8×8×1 k-mesh in monolayer for: (a) the band gaps; (b) the band-edge energies (VBM and CBM) of PE configurations; (c) the band-edge energies (VBM and CBM) of FE configurations; (d) the energy difference (ΔE, eV) between PE and FE.

D. Band structures and band gaps of 2D Bi₂OS₂.

Fig. S5 displays PBE-calculated band structures for the PE structures of bilayer and trilayer at typical biaxial strain (-4%, 0% and 4%). The band-gap values extracted from

the band structures are listed in Table. S6. It is seen that the CBMs of bilayer and trilayer deviate a little from X point in k-space, with their energies slightly lower than the energy of the lowest conduction band at X (Fig. S5). The deviation changes the direct-gap character into an indirect gap feature. In a previous study, this small deviation was also predicted for Bi_2OS_2 bilayer and trilayer without strain,[8] indicating a consistent result with ours. The most noticeable impact of this deviation may lie in carrier dynamics. This kind of small deviation was also found in $MAPbI_3$ and was proposed as one of possible reasons for extended carrier lifetime and long carrier diffusion length in $MAPbI_3$.[9] For indirect gap semiconductors, the photoexcited electrons relax to the CBM whose lattice momentum is not in line with that of the VBM in k-space, suppressing the radiative recombination and thus prolonging the carrier lifetime and diffusion length.[9] In Bi_2OS_2 multilayers, indirect gap character may also enhance carrier lifetime and diffusion length in a similar way, which then influences the carrier dynamics and optoelectronic performance. A deep understanding of this problem calls for a systematic study on this topic which is beyond the scope of this work.

Band gaps calculated at PBE-level for 2D PE and FE Bi_2OS_2 at various strains are presented in Table. S6 and also displayed in Fig. 3 of the main text.

The CBM states of 6%-strained monolayer exhibit a different charge density distribution from those of other strains. Specifically, the CBM states localize in the surface [BiS_2] layer for the strain from -6% to 5% (Fig. 5e), giving rise to surface states. For 6%-strained structures (Fig. 5f), the CBM states reside in the middle [Bi_2O_2] layer of monolayer. To find out the reason why such a transition occurs, we calculate the orbital-projected band structures of monolayer for 6p orbitals of the Bi in the [BiS_2] layer and of the Bi^* in the [Bi_2O_2] layer at typical strains (0%, 4% and 6%), as shown in Fig. S6. The energy of the lowest conduction band at Γ ($E_{CB}(\Gamma)$), mainly contributed by 6p orbitals of the Bi^* in the [Bi_2O_2] layer, decreases more significantly than that of the lowest conduction band at X ($E_{CB}(X)$) with stretching the lattice, which is contributed by 6p orbitals of the Bi in the [BiS_2] layer. At a large tensile strain like 6%, the $E_{CB}(\Gamma)$ is lower than $E_{CB}(X)$ and become the CBM. Thus, the CBM states locate in the [Bi_2O_2] layer at 6% strain, which is different from other strains.
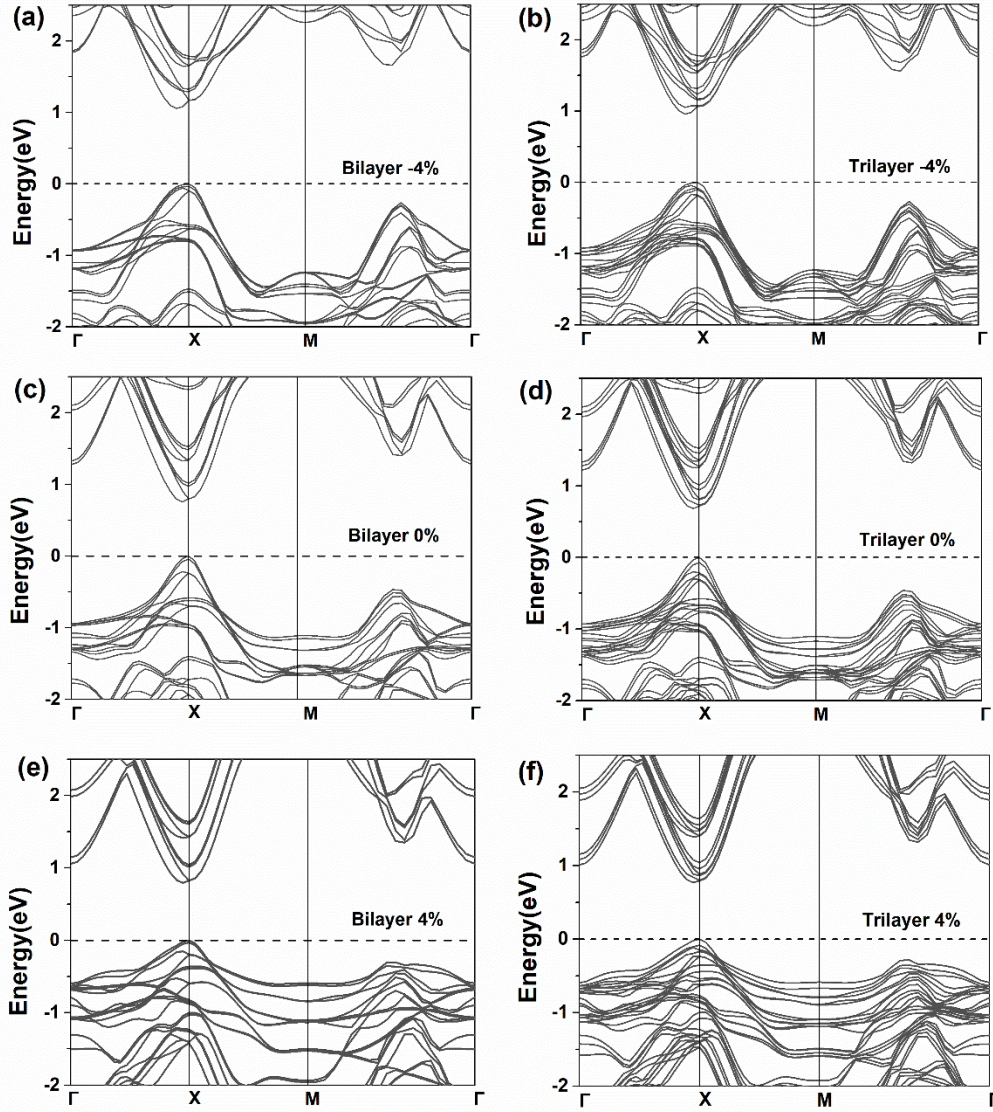
Fig. S5 PBE-calculated band structures for the PE structures of bilayer and trilayer at typical biaxial strain conditions: (a) and (b) for -4%, (c) and (d) for free-strain (0%), (e) and (f) for 4%. The energy of VBM is chosen as zero (horizontal dashed lines). The band-gap values extracted from the band structures are listed in Table. S6.

Table. S6 PBE-calculated band gaps (eV) of 2D PE and FE Bi_2OS_2 at various strains.

| Monolayer			Bilayer			Trilayer		
Strains	PE	FE	Strains	PE	FE	Strains	PE	FE
-0.06	1.67	1.67	-0.06	1.52	1.53	-0.06	1.42	1.48
-0.05	1.50	1.51	-0.05	1.32	1.33	-0.05	1.25	1.26
-0.04	1.34	1.35	-0.04	1.16	1.17	-0.04	1.06	1.10
-0.03	1.22	1.22	-0.03	0.99	1.01	-0.03	0.93	0.96
-0.02	1.11	1.12	-0.02	0.88	0.90	-0.02	0.79	0.83
-0.01	1.05	1.05	-0.01	0.83	0.85	-0.01	0.73	0.77
0	1.02	1.04	0	0.80	0.85	0	0.72	0.79
0.01	1.00	1.05	0.01	0.80	0.88	0.01	0.73	0.82
0.02	1.01	1.07	0.02	0.81	0.90	0.02	0.75	0.85
0.025	1.01	1.09	0.025	0.79	0.92	0.025	0.74	0.83
0.03	1.02	1.11	0.03	0.81	0.94	0.03	0.75	0.86
0.04	1.04	1.15	0.04	0.82	0.99	0.04	0.79	0.89
0.045	1.05	1.16	0.043	0.87	1.00	0.041	0.79	0.90
0.046	1.05	1.17	0.0435	0.85	0.93	0.043	0.78	0.87
0.047	1.05	1.16	0.044	0.87	0.93	0.045	0.81	0.86
0.048	1.06	1.10	0.045	0.87	0.94	0.047	0.80	0.87
0.049	1.06	1.10	0.047	0.87	0.92	0.049	0.82	0.88
0.05	1.06	1.10	0.049	0.86	0.94	0.05	0.82	0.87
0.06	1.06	1.10	0.05	0.85	0.92	0.06	0.87	0.88
			0.06	0.93	0.92			
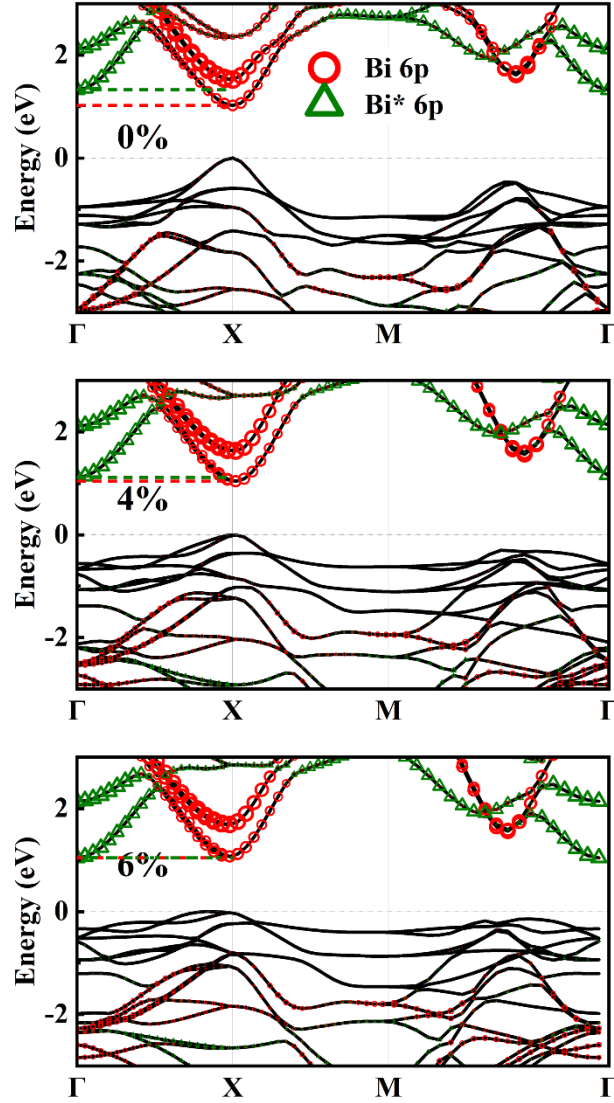
Fig. S6 Orbital-projected band structures of monolayer for 6p orbitals of the Bi in the [BS$_2$] layer and of the Bi* in the [Bi$_2$O$_2$] layer at typical strains (0%, 4% and 6%). The energy of the lowest conduction band at Γ(E_{CB}(Γ)), mainly contributed by 6p orbitals of the Bi* in the [Bi$_2$O$_2$] layer, decreases more significantly than that of the lowest conduction band at X (E_{CB}(X)) with stretching the lattice, which is contributed by 6p orbitals of the Bi in the [BiS$_2$] layer. For 0% strain, E_{CB}(Γ) is 0.305 eV higher than E_{CB}(X), while being slightly higher than E_{CB}(X) (0.076 eV) for 4% strain. At a large tensile strain like 6%, the E_{CB}(Γ) is 0.028 eV lower than E_{CB}(X) and become the CBM. The change of the energy difference with strain is clearly displayed by two horizontal dashed lines. This is the reason why the CBM states locate in the [Bi$_2$O$_2$] layer at 6% strain.

ESI Section S3: lattice misfit between freestanding [La$_2$O$_2$] (or [Bi$_2$O$_2$]) and [BiS$_2$] layers

The lattice misfit between freestanding [La$_2$O$_2$] (or [Bi$_2$O$_2$]) and [BiS$_2$] layers stand for the lattice mismatch between them in the **a-b** plane (in-plane). It is defined as (a_{La2O2}-a_{BiS2})/a_{BiS2} in LaOBiS$_2$ or (a_{Bi2O2}-a_{BiS2})/a_{BiS2} in Bi$_2$OS$_2$, where a is the in-plane lattice constants of [BiS$_2$], [Bi$_2$O$_2$] and [La$_2$O$_2$] layers. They are calculated by optimizing individual hypothetical [Bi$_2$O$_2$], [La$_2$O$_2$] and [BiS$_2$] layers which are cut from the LaOBiS$_2$ and Bi$_2$OS$_2$ monolayer. As shown in Fig. 1b, Bi$_2$OS$_2$ monolayer contains one [Bi$_2$O$_2$] layer and two [BiS$_2$] layers and can be broken into three freestanding layers. Similarly, LaOBiS$_2$ monolayer can be broken into one [La$_2$O$_2$] layer and two [BiS$_2$] layers. This method was used in a previous study to evaluate the lattice misfit between the [La$_2$O$_2$] layer and the [BiS$_2$] layer in LaOBiS$_2$.[10] The calculated constants are 3.861, 3.999 and 4.204 Å for freestanding [BiS$_2$], [Bi$_2$O$_2$] and [La$_2$O$_2$] layers, respectively. We note that the calculated in-plane constants of Bi$_2$OS$_2$ and LaOBiS$_2$ monolayer is 3.967 Å and 4.038 Å, respectively. Thus, the in-plane constant of Bi$_2$OS$_2$ monolayer (3.967 Å) is a compromise of one [Bi$_2$O$_2$] layer (3.999 Å) and two [BiS$_2$] layers (3.861 Å). Similarly, the in-plane constant of La$_2$OS$_2$ monolayer (4.038 Å) is also a compromise of one [La$_2$O$_2$] layer (4.204 Å) and two [BiS$_2$] layers (3.861 Å). Obviously, compared with [Bi$_2$O$_2$] layer, larger constant of [La$_2$O$_2$] layer makes the in-plane constant of La$_2$OS$_2$ larger than that of Bi$_2$OS$_2$. Then, the [BiS$_2$] layers are stretched more heavily in La$_2$OS$_2$ than in Bi$_2$OS$_2$. In other words, [La$_2$O$_2$] sustains a larger tensile strain for the [BiS$_2$] layers in LaOBiS$_2$ than [Bi$_2$O$_2$] does in Bi$_2$OS$_2$.

ESI Section S4: FE spontaneous polarization and ion displacements

The FE spontaneous polarizations of 2D Bi$_2$OS$_2$ at various tensile strain conditions are tabulated in Table. S7. Table. S8 shows the ion displacements of Bi, Bi*, S$_{xy}$, S$_z$ and O along **b**-axis in the FE structures for Bi$_2$OS$_2$ monolayer at the strain from 3% to 6%. Table. S9 displays the ion displacements along **b**-axis in the FE structures for LaOBiS$_2$ monolayer at 0% and 6% strains. Table. S10 presents the FE polarizations for monolayer calculated by using two force tolerances of 0.01 eV/Å and 0.001 eV/Å at typical +2% and +6% strain.

As shown in Table. S7 and S8, small net displacements for both Bi and S ions give rise to small relative cation-anion displacements and low FE polarization for the strain from 3% to 4.7 %. Large net displacements for both cation and anion but along opposite directions lead to large relative cation-anion displacements and thus large FE polarization for the strain higher than 4.8%. The complex trends of strain-dependent displacements are due to two kinds of coordination environments for both Bi (Bi and Bi*) and S (S$_{xy}$ and S$_z$) ions in Bi$_2$OS$_2$. We use the same initial displacements of ions in the unrelaxed structures for all strains, i.e., 0.08 Å for Bi cations, and -0.08 Å for S and O anions. This precludes the possibility that the complex trends are caused by different setting of initial ion displacements in the structures before relaxation. Furthermore, we obtain the same trends by using a vdW functional, optPBE-vdW (Fig. S1). In a previous study, Fu et al. also observed a non-monotonous trend of the polarization with the

tensile strain from 2% to 5% for Bi_2OS_2 monolayer.[11] However, they did not analyze the origin of the trends.

To check the convergence of FE properties with respect to force tolerance, we also calculate the FE polarizations at typical +2% and +6 % strains for monolayer by using a higher accuracy of the force tolerance of 0.001 eV/Å. The results from two force tolerances (0.01 and 0.001 eV/Å) are presented together in Table. S10. It is seen that the relative errors are 0.62% and -0.08% for +2% and +6 % strains, respectively, indicating that a force tolerance of 0.01 eV/Å is accurate enough to ensure the convergence of FE polarizations. As discussed in **ESI Section S2B,** a force tolerance of 0.01 eV/Å is accurate enough to ensure the convergence of the band gaps. All in all, a force tolerance of 0.01 eV/Å is accurate enough to ensure the convergence of our results. Actually, a force tolerance of 0.01 eV/Å is widely used in the DFT calculations.

For compressively strained 2D Bi_2OS_2, we built unrelaxed FE structures with the same initial displacements of ions (i.e., FE distortions) as those of tensile-strained Bi_2OS_2. After structural relaxation, FE distortions disappear and these FE configurations are close to their PE structures. The energy differences (ΔE) are less than 10^{-3} eV per unit cell for compressive strains. In contrast, the ΔE values of typical tensile strains like 4% and 6% are considerably large (>0.1 eV per unit cell) (see Fig. 6a in main text). This is the reason why we obtain the conclusion that FE distortions are unfavorable in energy and PE structures are stable states for compressively strained 2D Bi_2OS_2. As discussed in main text, stereochemical activity of lone-pair electrons from Bi cations is responsible for FE distortion in Bi_2OS_2 and $LaOBiS_2$. In a previous study, Bu *et al.* found that the compression of the lattice can suppress the activity of lone-pair electrons and thus inhibit the structural distortions in a similar compound Bi_2O_2S.[12] For compressively strained 2D Bi_2OS_2, the disappearance of FE distortions may be attributed to the suppression of lone-pair electrons.

Table. S7 Calculated spontaneous polarizations (P_S, in the unit of 10^{-9} Cm^{-1}) of 2D Bi_2OS_2 at various tensile strain conditions.

Monolayer		Bilayer		Trilayer	
Strains	P_S	Strains	P_S	Strains	P_S
0	0.15	0	0.19	0	0.21
0.01	0.21	0.01	0.31	0.01	0.5
0.02	0.24	0.02	0.42	0.02	0.74
0.025	0.25	0.025	0.35	0.025	0.58
0.03	0.18	0.03	0.26	0.03	0.50
0.04	0.11	0.04	0.14	0.04	0.30
0.045	0.10	0.043	0.12	0.041	0.80
0.046	0.09	0.0435	1.32	0.043	1.87
0.047	0.09	0.044	1.33	0.045	1.93
0.048	0.65	0.045	1.35	0.047	1.97
0.049	0.65	0.047	1.38	0.049	2.04
0.05	0.67	0.049	1.40	0.05	2.06
0.06	0.73	0.05	1.42	0.06	2.17
		0.06	1.57		

Table. S8 Ion displacements of Bi, Bi[*], S_{xy}, S_z and O along **b**-axis in the FE structures for Bi_2OS_2 monolayer at the strain from 3% to 6%. Symbols Bi and Bi[*] indicates the Bi atoms in the [BiS_2] and [Bi_2O_2] layers, respectively. The positions of these atoms are displayed in Fig. S2. In a unit cell, there are two sets of these atoms (Z=2).

Strains	3%	4%	4.5%	4.6%	4.7%	4.8%	4.9%	5%	6%
a/b (Å)	4.086	4.126	4.146	4.150	4.153	4.157	4.161	4.165	4.205
Bi	0.157	0.241	0.275	0.290	0.291	0.094	-0.052	-0.076	-0.078
Bi[*]	-0.129	-0.241	-0.280	-0.298	-0.298	0.043	0.309	0.343	0.395
S_{xy}	-0.130	-0.094	-0.083	-0.071	-0.074	-0.265	-0.419	-0.456	-0.494
S_z	0.051	0.081	0.087	0.089	0.087	0.015	-0.040	-0.036	-0.062
O	-0.030	-0.069	-0.082	-0.093	-0.089	0.031	0.119	0.142	0.154

Table. S9 Ion displacements along **b**-axis in the FE structures for $LaOBiS_2$ monolayer at 0% and 6% strains. Bi and S (S_{xy} and S_z) are in the [BiS_2] layer, and La and O are in the [La_2O_2] layer.

	$LaOBiS_2$	
Strains	0%	6%
Bi	0.030	0.207
La	0.004	-0.050
S_{xy}	-0.208	-0.248
S_z	0.007	-0.043
O	0.005	-0.038

Table. S10 FE polarizations (10^{-9} Cm^{-1}) for monolayer calculated by using two force tolerances of 0.01 eV/Å and 0.001 eV/Å at typical +2% and +6% strain. The relative errors (Δ_R, %) are also listed in the last row.

Force tolerances (eV/Å)	+2%	+6%
0.01	0.2431	0.7306
0.001	0.2416	0.7312
Δ_R (%)	0.62	-0.08

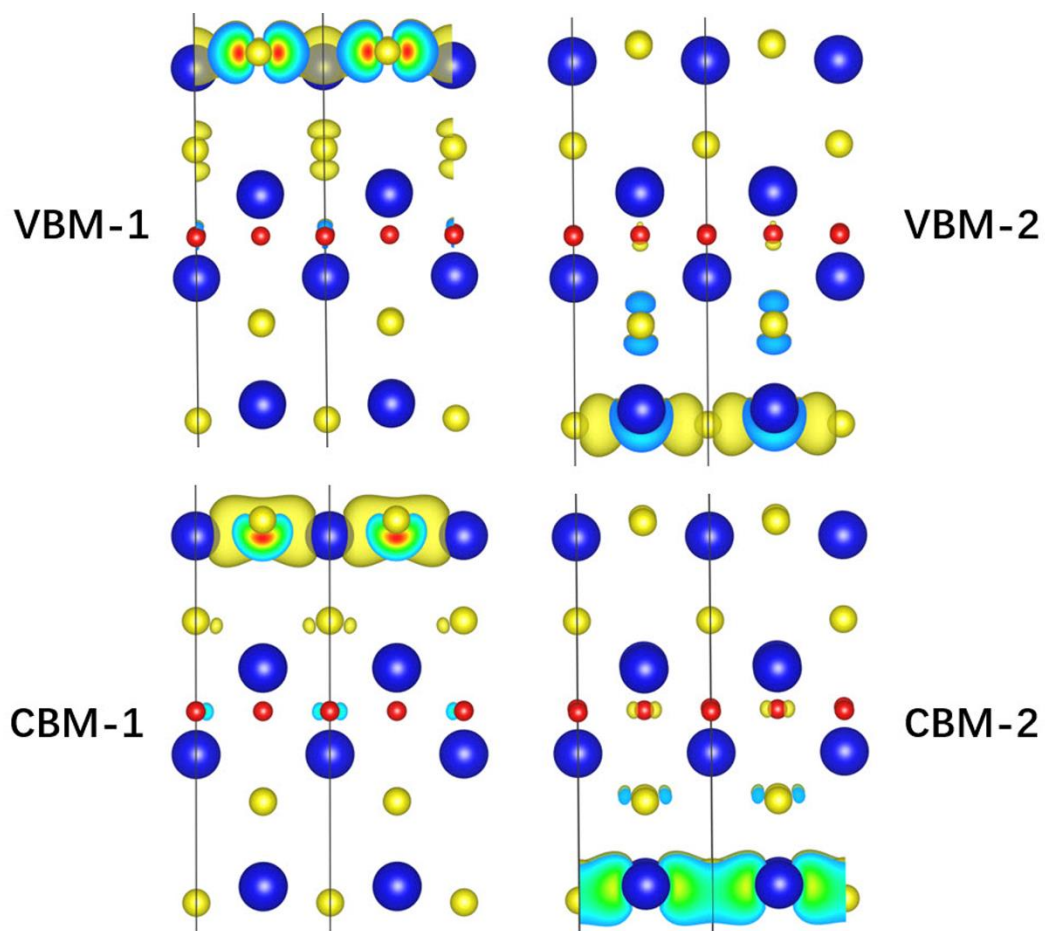**ESI Section S5: charge density and COHP**

Fig. S7 Charge density distribution of VBM and CBM states for free-strain monolayer. Both VBM and CBM are double-degenerate due to the symmetry. The charge densities of two highest valence bands at X point (denoted as VBM-1 and VBM-2) are distributed separately in two [BiS_2] layers. Similar distribution occurs to two lowest conduction bands at X (denoted as CBM-1 and CBM-2). Charge densities are shown with an isosurface level of 0.01e r_B^{-3} (r_B: Bohr radius).
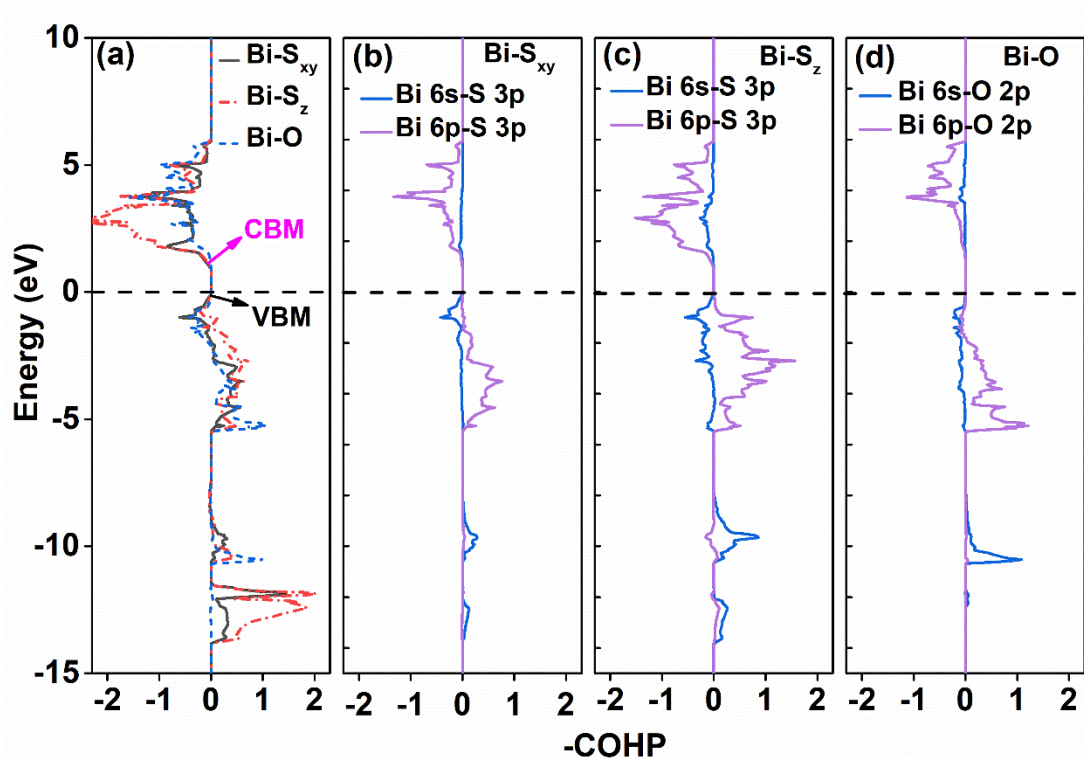
Fig. S8 Crystal orbital Hamilton population (COHP) of Bi-S$_{xy}$, Bi-S$_z$ and Bi-O bonds for Bi$_2$OS$_2$ monolayer. The sum of orbital interactions for each kind of bond are presented in (a). Bi 6s-S 3p and Bi 6p-S 3p populations are shown in (b), (c). Bi 6s-O 2p and Bi 6p-O 2p populations are shown in (d). By convention we plot negative COHP (-COHP) so that the positive (or negative) part of -COHP indicates the bonding (or antibonding) states. It is seen that the -COHP of band edge states, either for the VBM (black arrow) or the CBM (magenta arrow), is negative, which suggests that both VBM and CBM are of antibonding character.

References

1. S. Grimme, J. Antony, S. Ehrlich and H. Krieg, *J. Chem. Phys.*, 2010, **132**, 154104.
2. M. Dion, H. Rydberg, E. Schroder, D. C. Langreth and B. I. Lundqvist, *Phys,. Rev. Lett.*, 2004, **92**, 246401.
3. J. Klimeš, D. R. Bowler and A. Michaelides, *J. Phys.-Condens. Mat.*, 2010, **22**, 022201.
4. A. Miura, Y. Mizuguchi, T. Takei, N. Kumada, E. Magome, C. Moriyoshi, Y. Kuroiwa and K. Tadanaga, *Solid State Commun.*, 2016, **227**, 19-22.
5. B. Cordero, V. Gómez, A. E. Platero-Prats, M. Revés, J. Echeverría, E. Cremades, F. Barragán and S. Alvarez, *Dalton T.*, 2008, 2832-2838.
6. S. S. Batsanov, *Inorg. mater.*, 2001, **37**, 871-885.
7. A. R. Zanatta, *Sci. Rep.*, 2019, **9**, 11225
8. X. Zhang, B. Wang, X. Niu, Y. Li, Y. Chen and J. Wang, *Mater. Horiz.*, 2018, **5**, 1058-1064.
9. C. Motta, F. El-Mellouhi, S. Kais, N. Tabet, F. Alharbi and S. Sanvito, *Nat. Commun.*, 2015, **6**, 7026.

10. C. He, J. Zhu, Y.-H. Zhao, C. Liu and B. Fu, *Nanoscale*, 2019, **11**, 18436-18443.
11. B. Fu, D.-S. Ma, C. He, Y.-H. Zhao, Z.-M. Yu and Y. Yao, *Phys. Rev. B*, 2022, **105**, 035126.
12. K. Bu, H. Luo, S. Guo, M. Li, D. Wang, H. Dong, Y. Ding, W. Yang and X. Lü, *J. Phys. Chem. Lett.*, 2020, **11**, 9702-9707.